Received: 2 October 2025 | Revised: 12 December 2025 | Accepted: 18 December 2025

DOI: 10.1002/alz.71127

Alzheimer's & Dementia®
THE JOURNAL OF THE ALZHEIMER'S ASSOCIATION

RESEARCH ARTICLE

Impaired adrenergic regulation of Kv channels underlies LC hyperactivity and early-onset sleep disruption in AD-like amyloidogenic mice

Yi-Ci Zhang[1,2] | Xue-Ting Zhang[1,2] | Peng-Yue Chen[1,2] | Zi-Yue Zhou[1,2] | Mao-Qing Huang[1,2] | Kai-Wen He[1,2,3]

[1]Interdisciplinary Research Center on Biology and Chemistry, Shanghai Institute of Organic Chemistry, Chinese Academy of Sciences, Shanghai, China

[2]University of Chinese Academy of Sciences, Beijing, China

[3]Shanghai Key Laboratory of Aging Studies, Shanghai, China

Correspondence: Kai-Wen He, Interdisciplinary Research Center on Biology and Chemistry, Shanghai Institute of Organic Chemistry, Chinese Academy of Sciences, 100 Haike Rd. Shanghai 201203, China.
Email: kwhe@sioc.ac.cn

Funding information
Shanghai Science and Technology Development Funds, Grant/Award Number: 22ZR1475100; NSFC, Grant/Award Numbers: 32271004, 32070963; Lingang Laboratory, Grant/Award Number: LG-ADB410101; Shanghai Municipal Science and Technology Major Project, Grant/Award Number: 2019SHZDZX02

Abstract

INTRODUCTION: Sleep–wake disturbances frequently occur at early stages of Alzheimer's disease (AD) and accelerate disease progression, but the underlying neural mechanisms are not fully understood.

METHODS: We examined sleep–wake behavior and locus coeruleus (LC) activity in young 5xFAD mice using electrophysiology and pharmacological approaches targeting adrenergic signaling and potassium channels.

RESULTS: 5xFAD mice displayed dark phase–specific hyperarousal and impaired brain state transitions by 2 months of age. LC neurons exhibited increased tonic firing due to impaired Kv4 and Kv7 potassium channel conductance, resulting from soluble amyloid beta (Aβ)-induced disruption of α2A adrenergic receptor regulation. Pharmacological activation of α2A adrenergic receptors restored Kv4/7 function and normalized LC excitability. Local administration of guanfacine (α2A agonist) or retigabine (Kv7 modulator) significantly rescued sleep–wake disturbances.

DISCUSSION: These findings identify LC hyperexcitability as a mechanistic driver of early sleep disruption in AD and implicate α2A receptors and Kv7 channels as promising therapeutic targets for early intervention.

KEYWORDS
guanfacine, hyperexcitability, Kv4, Kv7, locus coeruleus, retigabine, sleep, α2A adrenergic receptor

Highlights

- Sleep–wake rhythm disruption is an early hallmark of AD.
- The LC, one of the earliest AD-vulnerable regions, drives dark phase–specific hyperarousal and impaired brain state transitions in young 5xFAD mice.

- Soluble Aβ-induced impairment of α2A adrenergic receptor regulation of the Kv4 and Kv7 potassium channels underlies LC hyperexcitability.
- Pharmacological restoration of α2A–Kv4/7 signaling normalizes LC activity *ex vivo* and rescues sleep–wake disturbances in vivo.
- Targeting α2A receptors and Kv7 channels represents a potential strategy for early intervention in AD-related sleep disruption.

1 | INTRODUCTION

Sleep–wake disturbances such as hyperarousal and shortened sleep are commonly observed in patients with Alzheimer's disease (AD).[1–4] Notably, mounting evidence from longitudinal studies and meta-analyses suggests that sleep disruption during the preclinical phase of AD is not merely a symptom but may actively contribute to the pathogenesis of the disease. Therefore, early sleep disturbances are increasingly recognized as a modifiable risk factor for AD.[1,3,5] However, the underlying mechanisms driving these early alterations in sleep–wake regulation remain poorly understood.

The locus coeruleus (LC), a small pontine nucleus composed predominantly of tyrosine hydroxylase-positive (TH+) noradrenergic neurons, plays a central role in regulating arousal, sleep–wake transitions, and attention.[6–9] Optogenetic activation of LC neurons has been shown to promote wakefulness and suppress non-rapid eye movement (NREM) sleep in a frequency-dependent manner.[10] Beyond its well-established role in initiating arousal, recent studies have highlighted the nuanced, state-dependent dynamics of LC neuronal activity that gate transitions between brain states. Moreover, prolonged activation of LC neurons leads to activity-dependent fatigue mediated by α2A-adrenergic receptor (α2A-AR)–driven auto-inhibition, contributing to the buildup of sleep pressure.[11]

Importantly, the LC is also one of the earliest and most vulnerable brain regions affected in AD. *Post mortem* and in vivo imaging studies reveal extensive LC degeneration that correlates with both disease severity and cognitive decline in AD patients.[12–14] Notably, pathological changes in the LC can occur decades before the onset of clinical symptoms,[15,16] raising the possibility that early LC dysfunction contributes to the earliest stages of AD progression, including sleep disturbances. However, how such early LC abnormalities arise – and their precise consequences for behavior – remains largely unexplored.

In this study, we investigated the relationship between early LC dysfunction and sleep–wake disturbances using 2-month-old 5xFAD mice, a widely used transgenic model of AD amyloidosis that exhibits early Aβ accumulation but minimal neurodegeneration or cognitive decline at this age. We found that young 5xFAD mice display marked hyperarousal and reduced brain state transitions, particularly during the dark phase. Electrophysiological analyses revealed a dark phase–selective hyperexcitability of LC neurons, driven by impaired α2A-AR-mediated modulation of Kv4 and Kv7 potassium channel conductance downstream of accumulated soluble amyloid beta (Aβ) at this early stage. Pharmacological enhancement of either α2A-AR or Kv7 activity locally in the LC was sufficient to restore normal sleep–wake patterns in these mice.

Together, our findings identify a previously unrecognized mechanism linking early LC hyperactivity to disrupted sleep architecture in the preclinical phase of AD. These results underscore the critical role of noradrenergic dysfunction in early disease-related behavioral phenotypes and suggest that targeting LC excitability may offer a novel therapeutic strategy for early intervention in Alzheimer's disease.

2 | METHODS

2.1 | Animals

All procedures were approved by the Institutional Animal Care and Use Committees at the Interdisciplinary Research Center on Biology and Chemistry, Chinese Academy of Sciences. Mice were group-housed under a 12 h:12 h light/dark cycle with ad libitum access to food and water. Male 5xFAD mice (B6.Cg-Tg(APPSwFlLon, PSEN1*M146L*L286V)6799Vas/Mmjax, originally from Jackson Laboratory) with their wild-type (WT) littermates were utilized in this study. For all experiments except those in Figure S1A–F (12 months) and Figure S1G,H (7 months), mice 2 to 3 months of age were used.

2.2 | Polysomnography recording

Polysomnography recording was carried out as described previously.[17] Briefly, mice were anesthetized by isoflurane vapor (1% to 2%) and head-fixed. The skull was exposed and two epidural screws were implanted (B: +1.5 to −3 mm, L: +1.5 mm). Two insulated stainless-steel wires bared at the tip region were implanted into the dorsal right and left neck muscles and sutured in place to record the electromyogram (EMG). All electrodes were connected to a four-pin socket connector that was cemented to the skull. Skin was sutured back, the wound was treated with triple antibiotic ointment, and the mice were allowed to recover in their home cage for at least 10 days prior to recordings.

During recording, mice were transferred to the customized chamber a day before the recording for habituation. Electroencephalogram (EEG) and EMG signals were recorded continuously depending on

RESEARCH IN CONTEXT

1. **Systematic review**: We searched PubMed and Google Scholar using terms including *Alzheimer's disease*, *sleep disruption*, *locus coeruleus*, *adrenergic signaling*, and *potassium channels*. Sleep–wake disturbances are established early features of AD, and the LC is among the first regions affected, yet the mechanisms underlying LC dysfunction and its contribution to sleep pathology remain poorly defined. While adrenergic modulation of LC excitability has been implicated, the specific ion channel mechanisms linking early amyloid pathology to LC hyperactivity have not been systematically explored.
2. **Interpretation**: Our study demonstrates that early amyloid pathology in 5xFAD mice induces dark phase–specific hyperarousal and impaired brain state transitions through LC hyperexcitability. We identify impaired α2A-adrenergic receptor activation – triggered by early amyloid accumulation – as a key mechanism that further disrupts Kv4 and Kv7 channel regulation. Pharmacological restoration of this signaling pathway effectively normalizes LC activity and rescues the associated sleep disturbances.
3. **Future directions**: Future studies should assess whether similar deficits in α2A–Kv signaling occur in humans and explore whether targeting this pathway can prevent or delay sleep and cognitive symptoms in prodromal AD.

experiments. Regular 12 h:12 h light/dark cycle was maintained with ad libitum access to food and water. EEG and EMG signals were sampled at 256 Hz with 1000 times preamplifier gain and bandpass filtered at EEG: 0.3 to 1000 Hz, EMG: 1 to 5000 Hz. All signals were acquired by Sirenia Acquisition NiDAQ 1.7.9 (Pinnacle Technology).

For sleep deprivation, mice were kept awake by gentle handling during the first 4 h (ZT0-4) and allowed to sleep ad libitum during the remaining 8 h of that light cycle. EEG/EMG signals were acquired continuously.

To evaluate the effect of retigabine on sleep, 20 mg/kg of retigabine was administered by intraperitoneal (IP) injection approximately 30 min before the onset of ZT12, followed by a complete 24h EEG/EMG recording. The same volume of vehicle was IP injected and the following EEG/EMG data from the same mouse was used as control.

2.3 | Cannula implant

To monitor sleep with LC local drug application, bilateral cannula targeting the LC area together with EEG/EMG electrode were implanted. A bilateral cannula was placed 200 µm above the LC with the following settings: Bregma, −5.45 mm; lateral, ± 0.88 mm; depth, −2.6 mm. All mice returned to their home cages after surgery and were monitored every day for a week. Further, 4 µg retigabine (2 µg/µl) or 5.6 ng guanfacine (2.8 ng/µl) was infused into LC of each hemisphere approximately 30 min to 1 h prior to ZT12 slowly via a microsyringe (Hamilton).

2.4 | Slice electrophysiology

2.4.1 | Acute brain slice preparation

Acute brain slices for electrophysiology were prepared as described previously[18,19] at ZT22 or ZT9. Briefly, all mice were anesthetized with isoflurane vapor and transcardially perfused with approximately 10 mL of ice-cold dissection buffer containing the following: 93 mM NMDG, 2.5 mM KCl, 1.2 mM $NaH_2PO_4{\cdot}2H_2O$, 30 mM $NaHCO_3$, 20 mM HEPES, 5 mM sodium ascorbate, 2 mM Thiourea, 3 mM sodium pyruvate, 25 mM D-Glucose, 12 mM NAc, 10 mM $MgCl_2$, 0.5 mM $CaCl_2$ bubbled with 95% O_2/5% CO_2. At the end of perfusion, mice were rapidly decapitated and whole brain was removed. Acute coronal brain slices 300 µm thick containing the LC were sectioned by a vibratome (1200S, Leica) in ice-cold dissection buffer. Slices were incubated in dissection buffer preheated to 30°C for 15 min and then transferred to artificial cerebrospinal fluid (ACSF) containing 119 mM NaCl, 5 mM KCl, 1.25 mM NaH_2PO_4, 1 mM $MgCl_2$, 2 mM $CaCl_2$, 26 mM $NaHCO_3$, and 10 mM Dextrose, saturated with 95% O_2 and 5% CO_2). Slices were then allowed to recover in ACSF at room temperature for at least 1 h before recording.

2.4.2 | Whole-cell recording

For whole-cell recordings, slices were transferred to a recording chamber continuously perfused with 30 ± 0.5°C ACSF at 2 mL/min. LC neurons were visualized by an upright fluorescence microscope (XT640-W, Olympus) and identified based on their localization and morphology. Borosilicate glass pipette recording electrodes with 3 to 6 MΩ tip resistance were filled with K^+-based internal solution (130 mM K-gluconate, 10 mM KCl, 10 mM HEPES, 0.2 mM EGTA, 0.5 mM Na_3GTP, 4 mM MgATP, 10 mM Na-phosphocreatine) adjusted to pH 7.2 to 7.4, 285 to 300 mOsm. Cells with a membrane resistance (Rm) > 100 MΩ and access resistance (Ra) < 25 MΩ were recorded. For all whole-cell recordings, cells were discarded if these values changed more than 25% during the experiment. Data were filtered at 2 kHz and digitized at 10 kHz using Clampex (Axon).

a) Spontaneous firing

To measure spontaneous firing, cells were held at resting membrane potential with no current injection, and spontaneous discharge was recorded continuously for at least 30 s. Only cells with resting membrane potential < −40 mV, Ra < 25 MΩ, and Rm > 100 MΩ were used for analysis.

b) Spontaneous excitatory postsynaptic currents (sEPSCs) and neuronal excitability

Recordings were done as previously described.[19,20] Both sEPSCs and excitability were recorded with regular ACSF without additional drugs. sEPSCs were recorded when cells were held at −60 mV in voltage clamp mode. To measure neuronal excitability, cells were current-clamped at −65 mV. Action potential threshold membrane potential and rheobase were estimated by injecting 500-ms ramp current from 0 to 400 pA. Maximal firing rate was measured by inject 500-ms current steps (0 to 1700 pA with 100 pA as step size). Only cells with resting membrane potential < −45 mV, Ra < 25 MΩ, and Rm > 100 MΩ were used.

c) Miniature inhibitory postsynaptic currents (mIPSCs)

mIPSCs were recorded when cells were held at −70 mV in voltage clamp mode with ACSF containing 1 μM TTX, 100 μM DL-APV, and 20 μM CNQX. Recording electrodes were filled with mIPSC internal solution (130 mM CsCl, 8 mM NaCl, 0.2 mM CaCl2, 10 mM HEPES, 2 mM EGTA, 0.5 mM Na_3GTP, 4 mM MgATP, 5 mM QX-314) adjusted to pH 7.2 to 7.3 with CsOH, 285 to 300 mOsm.

d) Voltage-gated potassium conductance

LC neurons were recorded in voltage clamp mode with K^+-based internal solution. The following drugs were added to the perfused ACSF to isolate Kv currents: 1 μM TTX, 100 μM DL-APV, 20 μM gabazine, and 20 μM CNQX. Total Kv currents were recorded by preholding cells at −120 mV for 750 ms followed by 400 ms step depolarization from −100 mV to +90 mV with 10 mV as step size. High-threshold Kv currents were estimated by preholding cells at −30 mV for 750 ms prior to depolarization steps (Figure 3A). Low-threshold Kv currents were calculated post hoc by subtracting high threshold Kv current from the total Kv current. Acute Kv currents were the maximal amplitude within 15 ms after current onset, whereas persistent Kv currents were measured as the plateau amplitude at the end of each current step. For comparison, Kv current density was calculated by normalizing I_k to the membrane capacitance (Cm) of individual cells.

e) Drug application

Perfusion buffer containing 20 μM XE991, 20 μM retigabine, 500 nM Phrixotoxin-1, 20 μM U0126, or 10 μM NS5806 was used to evaluate the contribution of Kv7 or Kv4 channels to the Kv currents, excitability, and spontaneous firing. In addition, 10 μM guanfacine and clonidine or 300 nM BRL-44408 maleate was used to evaluate the contribution of α2A adrenergic receptor to the Kv currents, excitability, and spontaneous firing. Ramp infusion of 0 to 100 μM guanfacine was used to assess α2A adrenergic receptor function. Acute brain slices were pre-incubated in ACSF containing 50 nM Aβ oligomer at room temperature for 30 min before recording.

2.4.3 | Total Aβ measurement

Mice were anesthetized with isoflurane vapor and rapidly sacrificed. Brains were immediately removed. Brain tissues containing target regions were microdissected and weighed. Enzyme-linked immunosorbent assay (ELISA) kit specific for Aβ42 (Invitrogen, Catalog No.: KHB3441) was used to quantify total Aβ42 according to the manufacturer's instructions.

2.5 | Immunofluorescence staining and imaging

2.5.1 | Brain tissue preparation

Mice were anesthetized with isoflurane vapor and transcardially perfused with 5 mL PBS, followed by 10 mL 4% phosphate-buffered paraformaldehyde (PFA) for immunofluorescence. Brains were then removed and fixed overnight in PFA.

2.5.2 | Immunofluorescence (IF) staining

PFA-fixed brains were dehydrated in 20% phosphate-buffered sucrose for 1 day and 30% phosphate-buffered sucrose for 2 days before embedded in tissue freezing medium (Catalog No.14020108926, Leica) and rapidly frozen in liquid nitrogen. Twenty-micrometer-thick coronal brain slices containing LC or hippocampus were section by Cryostat (Leica, CM3050 S). For staining, the slices were first treated with frozen slice antigen retrieval reagent (Beyotime, Catalog No.: P0090). They were then blocked with PBS containing 3% Normal Donkey Serum (NDS), 0.3% Triton X-100 at room temperature for 1 h before incubated with primary antibodies (TH, 1:3000; NeuN, 1:2000; Kv4.2, 1:500 Kv7.2, 1:500; Kv7.3, 1:500; GFAP, 1:10000; Iba1, 1:1000, Adra2A, 1:1000) overnight at 4°C. After washing with phosphate buffer saline with 0.1% Tween 20 (PBST), slices were incubated with secondary antibodies at room temperature for 2 h. Slices were washed with PBST and then mounted on glass slide and allowed to air dry. Prolong Gold Antifade Mountant (Invitrogen, Catalog No.: P36930) was used to slow down bleaching of fluorescence. Amyloid plaque was stained using Thioflavin S in combination with a gradient ethanol treatment following the manual instructions.

All antibodies and materials used are listed in Table S1.

2.6 | Confocal imaging

All fluorescence signals were acquired using a spinning disk microscope (Dragonfly 200, Andor) connected to a camera (Zyla sCMOS, Andor) with a 20× air lens. The image resolution was *x*/*y*: 0.300903/0.301040 μm/pixel. Stack images were acquired for all images. Step size (μm) and thickness (μm) of all images were 0.5, 1.

2.7 | Tissue preparation, RNA extraction and bulk RNA sequencing

Mice were anesthetized with isoflurane vapor and rapidly sacrificed. Brain slices containing the LC region were collected by a vibratome (1200S, Leica) in ice-cold dissection buffer. LC regions were microdissected on ice with sterile disposable biopsy punch (Integra Lifesciences, Catalog No.: 33-31), then quickly frozen with liquid nitrogen and stored at −80°C until use. TRIzol Reagent (Invitrogen Life Technologies) was used to retrieve total RNA. RNA concentration and quality were determined using a NanoDrop spectrophotometer (Thermo Fisher Scientific). Only high-quality RNA samples (OD260/280 = 1.8 to 2.2, OD260/230 ≥ 1.9, RNA integrity number (RIN) ≥ 9.0) were used for the library and bulk RNA sequencing (Shanghai Personal Biotechnology Cp. Ltd.).

2.7.1 | Quantitative real-time polymerase chain reaction (qPCR)

For qPCR, after DNase treatment to remove genomic DNA, the reverse transcription reactions were performed using Hifair III 1st Strand cDNA Synthesis SuperMix kit (Yeason, Catalog No.: 11141ES60). The cDNA was then used for real-time qPCR using TB Green Premix Ex Taq II (Takara, Catalog No.: RR820A) with the QuantStudio 6 Flex Real-Time PCR system (Life Technologies). The qPCR data were calculated using the 2-ΔΔCt method. The mRNA levels of actin were used as an internal control to normalize the mRNA levels of genes of interest.

The following qPCR primers were used in this study: mActin-F, 5′- GTGTGATGGTGGGAATGGGT-3′; mActin-R, 5′-GCTGGGGTGTTGAAGGTCTC-3′; mTNFα-F: 5′- CCCTCACACTCAGATCATCTTCT-3′; mTNFα-R: 5′- GCTACGACGTGGGCTACAG-3′; mIL1α-F, 5′- CGAAGACTACAGTTCTGCCATT-3′; mIL1α-R, 5′- GACGTTTCAGAGGTTCTCAGAG′; mIL1β-F, 5′- GCAACTGTTCCTGAACTCAACT -3′; mIL1β-R, 5′- ATCTTTTGGGGTCCGTCAACT -3′; mIL6-F, 5′- TAGTCCTTCCTACCCCAATTTCC -3′; mIL6-R, 5′- TTGGTCCTTAGCCACTCCTTC -3′; mGfap-F, 5′- CGGAGACGCATCACCTCTG-3′; mGfap-R, 5′- AGGGAGTGGAGGAGTCATTCG-3′; mIba1-F, 5′- ATCAACAAGCAATTCCTCGATGA-3′; mIba1-R, 5′- CAGCATTCGCTTCAAGGACATA -3′; mKcnd2-F, 5′- GGGTGGATGCCTGTTGCTT-3′; mKcnd2-R, 5′- GTCTTGCCATGTCTGGAAACG-3′; mKcnq2-F, 5′- CTGCCTGGAGATTCTATGCTACT -3′; mKcnq2-R, 5′- AGTGACTGTCCGCTCGTAGT-3′; mKcnq3-F, 5′- GAGCCGACAAAGACGGGAC -3′; mKcnq2-R, 5′- TTGGCGTTGTTCCTCTTGACT -3′; mAdra2a-F, 5′- GTGACACTGACGCTGGTTTG -3′; mAdra2a-R, 5′- CCAGTAACCCATAACCTCGTTG -3′; mAdra2b-F, 5′- TCTTCACCATTTTCGGCAATGC -3′; mAdra2b-R, 5′- AGAGTAGCCACTAGGATGTCG -3′; mAdra2c-F, 5′- GACGCAAGCGGTAGAGTACA -3′; mAdra2c-R, 5′- GTAGAACGAGACGAGAGGCG-3′

3 | QUANTIFICATION AND STATISTICAL ANALYSIS

3.1 | Analysis of sleep–wake states

States of wakefulness, NREM, REM sleep, and microarousal were first automatically analyzed in 5-s epoch by NeuroScore (Data Sciences International) using the same criteria: slow wave ratio: 0.4, theta ratio: 3. The results were manually checked. Wake epochs shorter than 10 s were defined as microarousals.

3.2 | EEG signal processing and analysis

EEG signals were bandpass filtered at 0.5 to 100 Hz and power line filtered at 50 Hz before analyzed by Fourier Transform. The brain oscillation bands were defined as Delta (δ): 0.5-4 Hz, Theta (θ): 4-8 Hz, Alpha (α): 8-12 Hz, Beta (β): 12-30 Hz, $\text{Gamma}_{\text{low}}$ (γ_{low}): 30-50 Hz. The Unitary power was defined as average power per 5-second epoch. Each bout is defined as a continuous state of wake/ NREM/ REM with no interruptions for sleep structure analysis.

3.2.1 | sEPSCs and mIPSCs analysis

sEPSCs and mIPSCs were analyzed using the MiniAnalysis program (Synaptosoft, Decatur, GA, USA), as described previously.[19] The event detection threshold was set at three times over the root mean square (RMS) noise. At least 300 events with rise time <3 ms were selected for each cell to calculate sEPSC and mIPSC frequency and amplitude.

3.2.2 | Image analysis

Immunofluorescent images were batched analyzed by Fiji ImageJ (NIH) and Imaris (Oxford Instruments). All images were projected in the *z*-direction with maximum intensity followed by background subtraction. For intensity signals, LC neurons were identified by TH-positive signals and the positive region signals were measured. For Iba1-positive puncta density measurements, Iba1-positive puncta were automatically selected and counted by the Spot module of Imaris. All images were analyzed in a double-blinded manner. To report the IF results, the mean signal intensity was normalized to control groups. For different batches of experiments, groups were normalized to their own control before combination. The raw value of Iba1 puncta density was reported.

3.2.3 | Bulk RNA sequencing analysis

The Bioinformatics pipeline (https://github.com/emc2cube/Bioinformatics) was used to process sequencing data. STAR[21]

was used to align reads to mm39 genome build, and RSEM was used to quantify expression at the gene level.[22] Differential expression analysis was conducted using DESeq2 with default parameters.[23] Differential gene expression was identified using a statistical cut-off of *p*adj <0.05.

3.3 | Statistics

Sample size is indicated in all figures as mouse number or cell then mouse number. Statistical analysis was performed by Prism version 6.0 software (GraphPad Software, Inc.). Wilcoxon signed-rank test was used for paired data. Mann-Whitney U test was used for unpaired data. Two-way ANOVAs with Sidak post hoc multiple-comparisons test were used to compare current - voltage (I-V) curves and current - spiking curves. Error bars in all figures indicate the standard error of the mean (SEM). Significant comparisons were labeled in the figures. The level of significance was set at $p < 0.05$. $^{*}p < 0.05$; $^{**}p < 0.01$; $^{***}p < 0.001$; $^{****}p < 0.0001$. *P* values ($0.05 < p < 0.1$) are labeled in the graphs.

3.4 | Code availability

The customized MATLAB codes are available on GitHub.
https://github.com/KaiWen-Helab/Zhang_tau2024

4 | RESULT

4.1 | Early-onset sleep deficits in 5xFAD mice characterized by hyperarousal and reduced brain state transitions

Sleep disturbances are well documented in aged AD mouse models.[24–26] Consistent with these findings, we observed a significant reduction in both NREM and rapid eye movement (REM) sleep, along with increased wakefulness, in 12-month-old 5xFAD mice (Figure S1A–F and Table S2). These results, in line with prior studies, underscore the utility of transgenic AD models for studying the sleep dysfunction commonly associated with the disease.[3,27,28]

To explore the early sleep abnormalities, we examined 5xFAD mice at 2 months of age – an early disease stage marked by sparse amyloid deposition (Figure S1G,H), but without reported cognitive deficits.[29] At this stage, the sleep–wake architecture remained relatively normal and intact (Figure 1A–C). However, compared to WT littermates, 5xFAD mice exhibited prolonged wakefulness and decreased NREM sleep duration compared to their WT littermates, particularly during the dark phase (Figure 1D–F). This was accompanied by a decreased number of wake, NREM, and REM bouts (Figure 1G,I), as well as fewer transitions between wake–NREM and NREM–REM states (Figure S1J and Table S3) in the dark cycle, suggesting a state of hyperarousal and impaired flexibility in sleep–wake regulation.

Furthermore, young 5xFAD mice showed reduced NREM delta (δ, 0.5 to 4 Hz) power (Figures 1K–M and S1K), a phenotype observed in both AD patients and aged AD mouse models,[30] while maintaining relatively preserved sleep homeostasis (Figure S1L–O). Collectively, these findings demonstrate the emergence of sleep deficits as early as 2 months of age in 5xFAD mice, characterized by dark phase–selective hyperarousal, impaired state transitions, and decreased delta power.

4.2 | Dark phase–selective hyperactivity of LC neurons in young 5xFAD mice

To investigate the potential cause of early-onset sleep disturbances in young 5xFAD mice, we focused on the LC, a brainstem nucleus critical for sleep–wake regulation.[7] Activation of LC neurons promotes arousal.[10] Their activities were recently found to be important also for brain state transitions.[31] Moreover, the LC is among the first brain regions affected in AD.[16] Therefore, given the observed sleep phenotypes in young 5xFAD mice, we sought to examine LC neuron dynamics in young 5xFAD mice.

LC neurons act as pacemakers with low tonic firing rates that vary depending on brain states.[8] To assess their activity, we recorded tonic firing rates in acute brain slices collected during the dark phase (zeitgeber time [ZT] 22) and the light phase (ZT9) from 2-month-old 5xFAD mice and WT littermates. LC neurons were identified based on their location and morphology, with their identity confirmed via post hoc staining for TH and biotin filling (Figure 2A).

In the dark phase, LC neurons from 5xFAD mice exhibited significantly elevated tonic firing rates compared to WT controls despite the unchanged resting membrane potential (Figure 2B–D) and membrane resistance (Figure S2A). More than 65% of LC neurons in 5xFAD mice fired at rates exceeding 9 Hz compared to less than 10% in WT littermates (Figure 2C). This corresponded to a two-fold increase in average tonic firing rate in 5xFAD mice in the dark phase (Figure 2D, left panel). Notably, this hyperactivity was phase-selective: no difference in tonic LC firing rate was observed between genotypes in the light phase (Figure 2E–G). These findings align with the observed dark phase–selective sleep phenotypes and suggest that elevated LC activity may underlie the hyperarousal and impaired transition observed in young 5xFAD mice.

To determine whether the increased LC activity in the dark phase stemmed from altered synaptic inputs or neuronal excitability, we first assessed sEPSCs (Figure 2H) and mIPSCs (Figure 2I). Neither sEPSCs nor mIPSCs differed between young 5xFAD mice and their WT littermates, suggesting unaltered synaptic inputs at this age. We then assessed neuronal excitability. While threshold potentials were similar (Figure S2A,B), LC neurons in 5xFAD mice exhibited a slightly reduced rheobase (Figure S2C), significantly elevated maximal firing rate, and slower spike frequency accommodation in response to more depolarized current steps (Figure 2J–L). Unlike WT LC neurons, which reached their maximum firing rate with, on average, 500 pA current injection, many neurons in 5xFAD

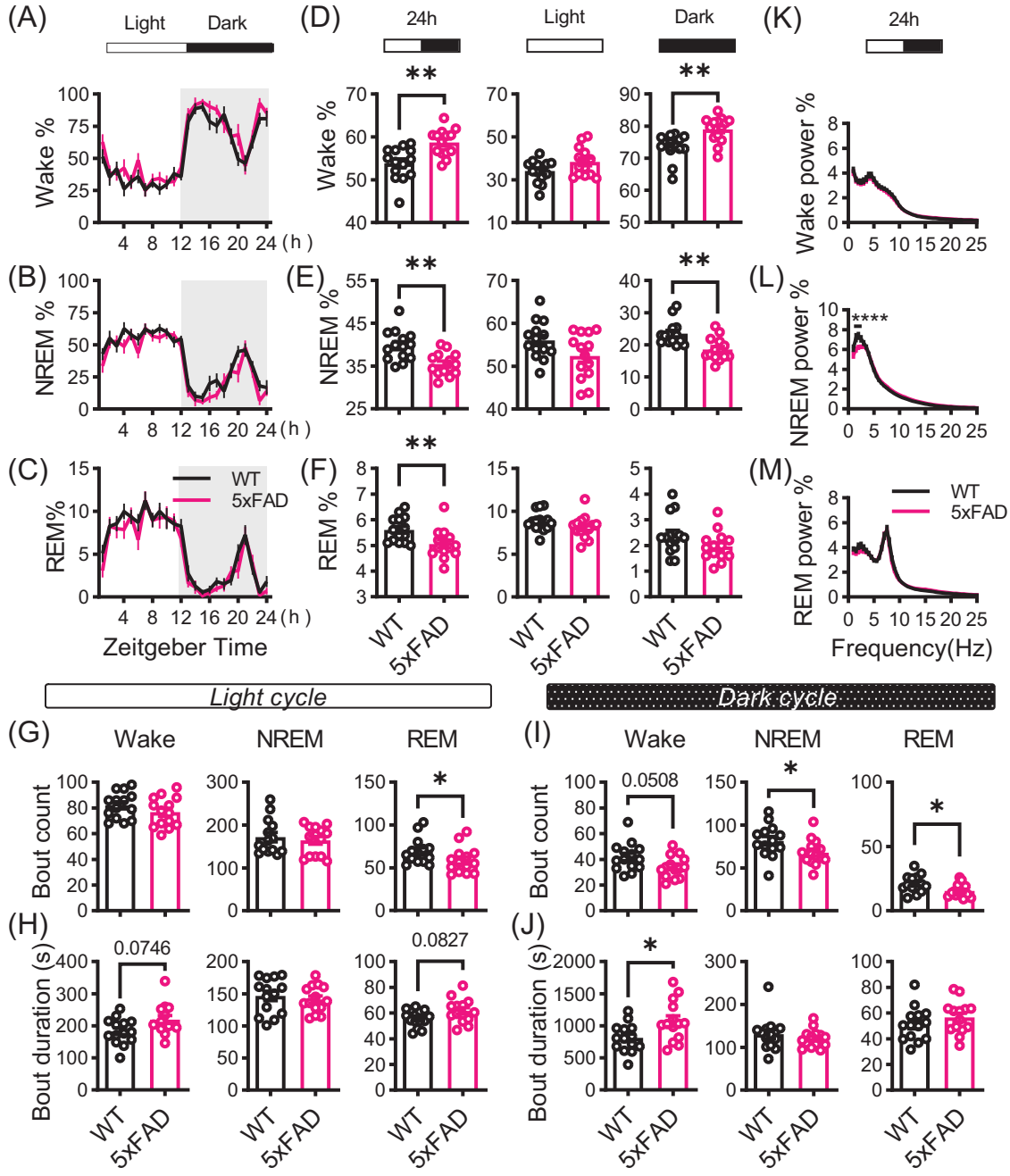

FIGURE 1 Early-onset sleep deficits in 2-month-old 5xFAD mice. (A–F) Percentages of time spent in wake (A), NREM sleep (B), and REM sleep (C) across the light/dark cycle in 2-month-old 5xFAD mice and their WT littermates. Comparisons of the percentage of time spent in wake (D), NREM (E), and REM (F) during 24-h day (left panels), light cycle (middle panels), and dark cycle (right panels) between 2-month-old 5xFAD mice and their WT littermates (WT: $n = 14$ mice; 5xFAD: $n = 14$ mice). Data shown in Table S2. (G–J) The differences in bout count number (G and I) and mean bout duration (H and J) for distinct vigilance stages during light cycle and dark cycle in comparisons of the 2-month-old 5xFAD mice to their WT controls. Left panels: wake; middle panels: NREM. Right panels: REM (WT: $n = 14$ mice; 5xFAD: $n = 14$ mice). Data shown in Table S2. (K–M) Comparison of normalized EEG power spectra of wake (K), NREM (L), and REM (M) during the 24-h day between 2-month-old 5xFAD mice and WT mice (WT: $n = 14$ mice; 5xFAD: $n = 14$ mice) (L), two-way ANOVA, $F(1, 26) = 0.1157$, $p = 0.7365$, Sidak post hoc multiple-comparisons $p < 0.0001$ at 1 to 2.5 Hz). Data are shown as mean ± SEM. Mann–Whitney tests were performed. EEG, electroencephalogram; NREM, non-rapid eye movement; REM, rapid eye movement; WT, wild type.

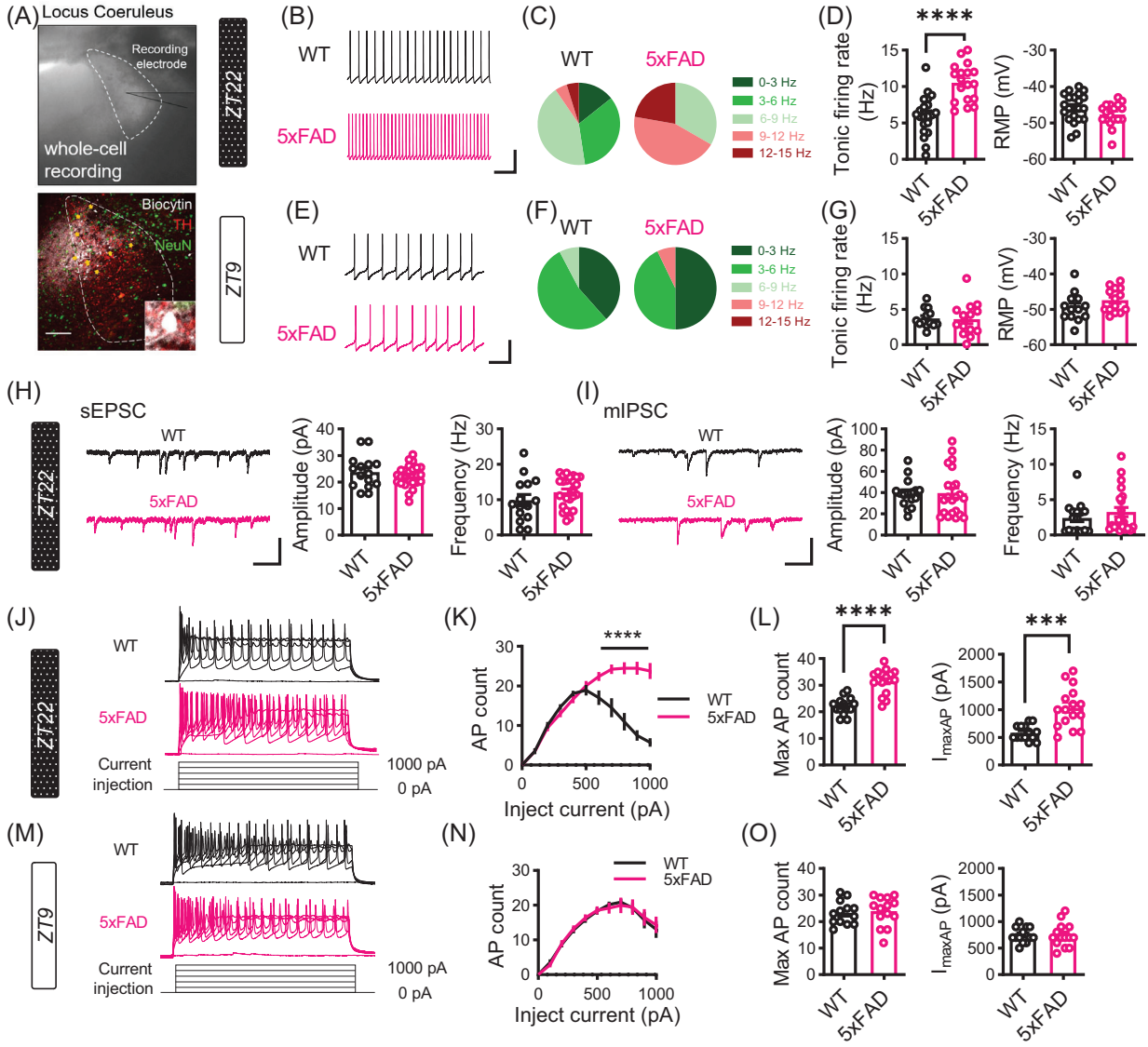

FIGURE 2 Dark phase–selective hyperactivity and hyperexcitability of LC neurons in 2-month-old 5xFAD mice. (A) Images showing whole-cell recording of LC neuron (upper panel) and post hoc staining to verify the TH+ cell identity (lower panel, biocytin: white; TH: red; NeuN: green. Scale bar, 100 μm). (B–G) *Ex vivo* recordings of tonic firing of LC neurons in 2-month-old 5xFAD mice and WT littermates at ZT22 (B–D), WT: 21 cells from three mice; 5xFAD: 18 cells from three mice) and ZT9 (E–G), WT: 13 cells from three mice; 5xFAD: 14 cells from three mice). (B and E) Representative traces of recording (scale bar, 600 ms, 25pA). (C and F) Distribution of firing rate. (D and G) Quantification of firing rate (left panels: panel D: ZT22, WT = 6.07 ± 2.72 Hz; 5xFAD = 10.53 ± 2.57 Hz; $p < 0.0001$; panel G: ZT9, WT = 3.73 ± 1.34 Hz; 5xFAD = 3.62 ± 2.38 Hz; $p = 0.6500$) and resting membrane potential (RMP, right panels: panel D: ZT22, WT = −45.76 ± 3.94 mV; 5xFAD = −47.67 ± 3.14 mV; $p = 0.1017$; panel G: ZT9, WT = −49.39 ± 4.05 mV; 5xFAD = −47.43 ± 3.39 mV; $p = 0.1630$). (H) Comparison of spontaneous EPSCs at ZT22 (WT: 15 cells from three mice; 5xFAD: 25 cells from three mice). Left panel, example sEPSC traces. Middle and right panels, quantification of the sEPSC amplitude (middle, WT = 23.78 ± 6.11 pA; 5xFAD = 22.28 ± 4.09 pA; $p = 0.6142$) and frequency (right, WT = 9.88 ± 6.17 Hz; 5xFAD = 12.14 ± 4.44 Hz; $p = 0.1310$) (scale bars, 50 pA, 250 ms). (I) Comparison of miniature IPSCs at ZT22 (WT: 16 cells from 3 mice; 5xFAD: 22 cells from 3 mice). Left panel, example mIPSC traces. Middle and right panels, quantification of mIPSC amplitude (middle) (WT = 39.32 ± 13.15 pA; 5xFAD = 39.69 ± 22.04 pA; $p = 0.4918$) and frequency (right) (WT = 2.41 ± 2.14 Hz; 5xFAD = 3.25 ± 3.04 Hz; $p = 0.2461$). (Scale bars, 50pA, 250 ms.) (J–O) Comparison of neuronal excitability at ZT22 (J–L), WT: 14 cells from three mice; 5xFAD: 16 cells from three mice) and ZT9 (M–O), WT: 13 cells from three mice; 5xFAD: 14 cells from three mice). (J and M) Representative traces evoked by injecting 500 ms current steps (0, 200, 400, 600, 800, 1000 pA). (K and N) Current-spiking relationship of LC neurons (K): ZT22, two-way ANOVA, $F(1, 28) = 43.24$, $p < 0.0001$, Sidak post hoc multiple-comparisons $p < 0.0001$ at 700 to 1000 pA; panel N: ZT9, two-way ANOVA, $F(1, 25) = 0.04$, $p = 0.8345$). (L and O) Quantification of maximum firing rate (left panels, panel L: ZT22, WT = 22.14 ± 3.28; 5xFAD = 31.50 ± 4.70; $p < 0.0001$; panel O: ZT9, WT = 23.31 ± 4.40; 5xFAD = 23.93 ± 5.48; $p = 0.5918$) and currents required to generate the maximum firing (I_{maxAP}, right panels, panel L: ZT22, WT = 585.71 ± 135.06 pA; 5xFAD = 1031.25 ± 360.96 pA; $p = 0.0001$; panel O: ZT9, WT = 746.15 ± 145.00 pA; 5xFAD = 742.86 ± 224.34 pA; $p = 0.8149$). Data are shown as mean ± SEM. Mann–Whitney tests were performed. EPSC, excitatory postsynaptic current; IPSC, inhibitory postsynaptic current; LC, locus coeruleus; mIPSC, miniature IPSC; sEPSC, spontaneous EPSC; TH, tyrosine hydroxylase; WT, wild type.

mice tolerated much higher injected current (I_{maxAP}, Figure 2L, right panel).

Importantly, these excitability changes were absent during the light phase (Figure 2 M–O), reinforcing the phase-selective nature of LC hyperactivity in young 5xFAD mice. Together, these data suggest that increased intrinsic excitability – rather than altered synaptic input – underlies the dark phase–specific hyperactivity of LC neurons and may contribute to early sleep–wake disturbances in this AD mouse model.

4.3 | Impaired low-threshold Kv4 and Kv7 conductance mediating LC neuronal hyperexcitability

Voltage-gated potassium (Kv) channels play a crucial role in the generation and maintenance of action potential.[32] Therefore, we investigated whether there were alterations in Kv channel conductance in the LC neurons of 5xFAD mice. Kv channels were categorized as either high-threshold (HT) or low-threshold (LT).[32] We recorded both total and HT K^+ current (I_k) by preholding at either −120 mV or −30 mV (Figure 3A, see Section 2, "Methods"). LT K^+ current was calculated post hoc by subtracting HT from total I_k (Figure 3B). Both acute (fast-kinetic, Figure 3B, gray arrowhead) and persistent (slow-kinetic, Figure 3B, black arrowhead) I_k amplitudes were quantified. LC neurons from 5xFAD mice showed a significant reduction in total I_k, including both acute (Figure 3C) and persistent components (Figure 3D). The HT K+ currents only showed mild changes (Figure 3E,F). In contrast, both acute (Figure 3G) and persistent (Figure 3H) LT K+ currents were significantly impaired. Kv4 and Kv7 channels, major contributors to LT acute and persistent currents, respectively,[32] are highly expressed in the LC (Figure S3A). We hypothesized that impaired Kv4 and Kv7 channel properties might underlie the hyperexcitability observed in LC neurons of 5xFAD mice. Pharmacological inhibition of Kv7 with XE991 in WT LC neurons reduced LT persistent K^+ conductance (Figure S3B), mimicking the phenotype of 5xFAD neurons and increased neuronal excitability in WT mice by elevating the maximum firing rate (Figure 3I). Similarly, selective inhibition of Kv4 channels using phrixotoxin-1 (PaTX1)[33] (Figure S3C) increased WT LC firing rates by preventing depolarization blockade (Figure 3J). The contribution of Kv4 to neuronal excitability was further supported by experiments using U0126, a MEK1/2 inhibitor that also potently blocks Kv4 channels[34,35] (Figure S3D–F). These results suggest that impaired Kv4 and Kv7 channels contribute to the slower accommodation and elevated maximum firing rate in the LC neurons of young 5xFAD mice. Indeed, co-application of Kv4 (NS5806) and Kv7 (retigabine) agonists restored LT I_k (Figure S3G) and mitigated the hyperexcitability of 5xFAD LC neurons (Figure 3K). Activation of Kv4 and Kv7 channels also rescued 5xFAD LC neuron hyperactivity (Figure 3L).

In summary, our findings demonstrate that impaired LT Kv channels, particularly Kv4 and Kv7, mediate the hyperexcitability and hyperactivity of LC neurons in young 5xFAD mice.

4.4 | Impaired α2A adrenergic receptor signaling drives LC hyperactivity via dysfunctional Kv4 and Kv7 channel conductance

The impaired Kv4 and Kv7 channel conductance observed in LC neurons of 5xFAD mice may stem from disrupted regulation rather than reduced expression. qPCR analysis (Figure S3H) and immunofluorescent labeling of major Kv4 and Kv7 subunits (Figure S3I–K) revealed no significant differences in mRNA or total protein levels between 5xFAD and WT mice. These results suggest that the functional impairment arises from altered modulation rather than transcriptional or translational deficits at the early stage.

Given that norepinephrine (NE) is the principal neurotransmitter released by LC neurons and that NE can exert feedback inhibition via α2-adrenergic autoreceptors located on both synaptic and somatic sites,[36,37] we explored the role of α2A-adrenergic receptor (α2A-AR) signaling. The α2A-AR subtype is highly enriched in the LC (Figure S4A), and its dysfunction was previously implicated in promoting LC hyperactivity.[38–40] To assess whether impaired α2A-AR signaling contributed to LC hyperactivity in young 5xFAD mice, we applied guanfacine, a selective α2A-AR agonist, during electrophysiological recordings. Guanfacine significantly reduced tonic firing rates of 5xFAD LC neurons to the WT level (Figure 4A), suggesting that insufficient endogenous α2A-AR activation contributed to the heightened firing observed in 5xFAD mice during the dark phase.

At the same time, guanfacine effectively suppressed the LC neuronal hyperexcitability in 5xFAD mice (Figure 4B,C), which was mediated by enhancing the low-threshold acute and persistent I_k (Figure 4D,E). This is in line with previously findings showing that α2-adrenergic receptor could modulate Kv7 channel activity.[41–43] These effects were replicated using clonidine, another α2-AR agonist, which similarly reduced neuronal hyperexcitability in 5xFAD mice (Figure 4F–H). Conversely, pharmacological blockade of α2A-ARs using BRL-44408 maleate in WT mice induced a hyperexcitable phenotype resembling that of 5xFAD neurons (Figure 4I–K). In contrast, neither guanfacine (Figure S4B–D) nor clonidine (Figure S4E–G) altered the physiological properties of WT LC neurons, consistent with a pre-activated state of α2A-ARs driven by elevated somatic NE release during the dark phase.

To directly compare the sensitivity of α2A-ARs between genotypes, we assessed the guanfacine dose–response at ZT9, when LC firing rates are low (Figure 2F,G) and α2A-ARs are expected to be largely unoccupied due to minimal NE release. Under these conditions, both WT and 5xFAD neurons exhibited guanfacine-induced suppression of firing (Figure S4H), confirming preserved α2A-AR–mediated inhibitory signaling. However, WT neurons displayed a faster onset and significantly greater magnitude of suppression than 5xFAD neurons (Figure S4H,I), indicating reduced α2A-AR activation efficacy in 5xFAD LC neurons. Consistent with a signaling rather than expression deficit, neither α2A-AR mRNA (Figure S4M) nor total protein levels (Figure S4N) differed between genotypes at 2 months of age.

Together, these results demonstrate that α2A-AR activation is functionally compromised in 5xFAD LC neurons, leading to decreased

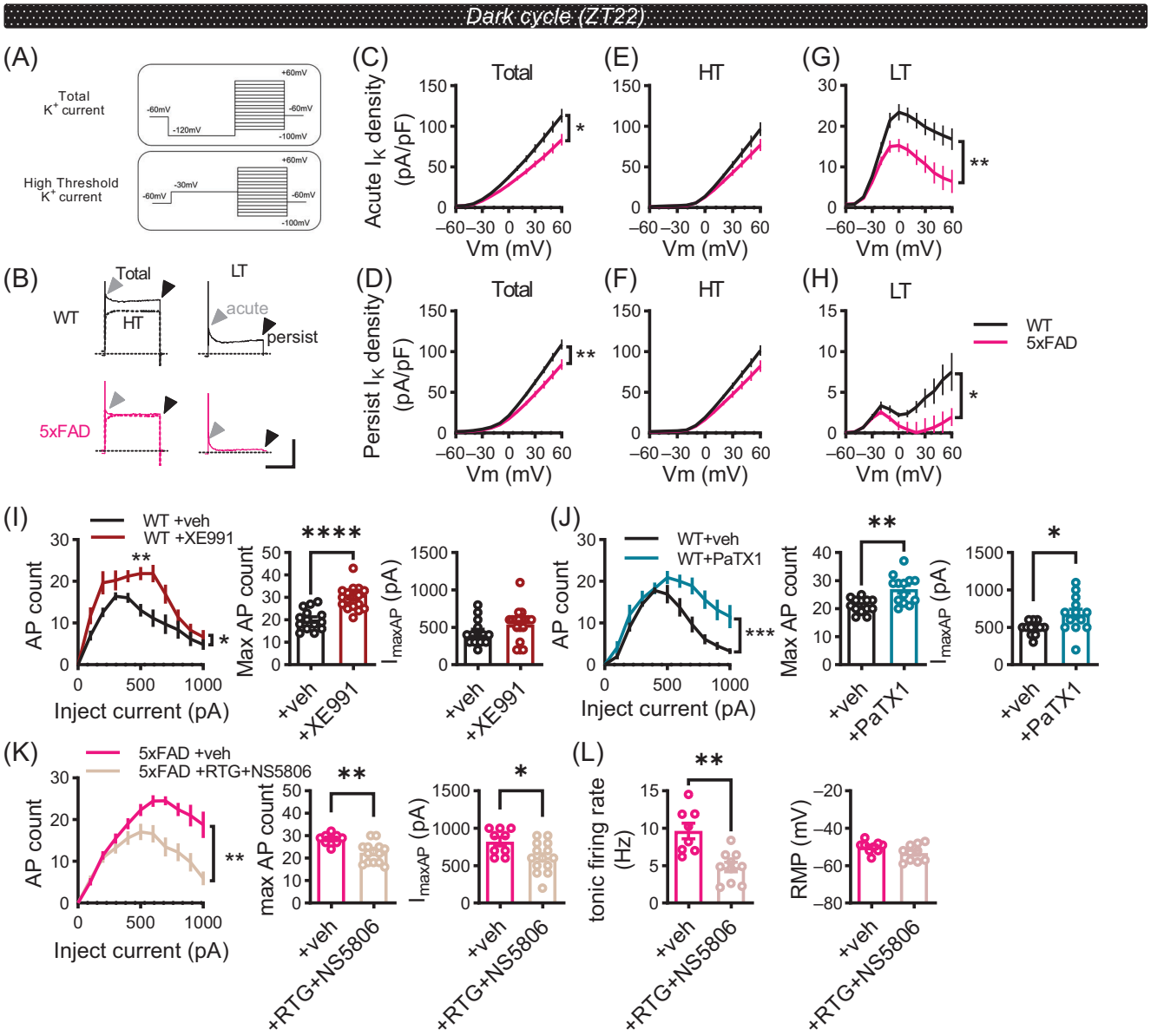

FIGURE 3 Downregulated Kv4 and Kv7 currents mediate elevated excitability and activity of LC neurons in young 5xFAD mice. (A) Diagram depicting protocols used for measuring the total voltage-gated I_k (upper panel) and HT voltagegated I_k (lower panel). (B–H) Comparison of Kv channel conductance of LC neurons between WT and 5xFAD (WT:12 cells from three mice; 5xFAD: 13 cells from three mice). (B) Right panels: example traces of total (solid traces) and HT (dotted traces) potassium current (I_k). Left panels: example traces of LT I_k. Gray arrowheads: acute I_k. Black arrowheads: persistent I_k. Scale bar: 2000 pA, 300 ms. (C–H) V–I_k curves of acute (C), (E), (G), and persistent (D), (F), (H) I_k density. Left panels, total I_k; middle panels, HT I_k; right panels, LT I_k. (Two-way ANOVA, panel C: $F(1, 23) = 7.796$; $p = 0.0104$; panel D: $F(1, 23) = 8.748$; $p = 0.0071$; panel E: $F(1, 23) = 3.021$; $p = 0.0956$; panel F: $F(1, 23) = 4.112$; $p = 0.0543$; panel G: $F(1, 23) = 9.977$; $p = 0.0044$; panel H: $F(1, 23) = 5.299$; $p = 0.0307$). (I and J) Effect of XE991 (I), Veh: 14 cells from four mice; XE991: 18 cells from three mice) or Phrixotoxin-1 (J), Veh: 12 cells from three mice; PaTX1: 13 cells from three mice) on neuronal excitability of LC neurons of WT mice. Left panels, current-spiking relationship (I), two-way ANOVA, $F(1, 30) = 7.064$, $p = 0.0125$, Sidak post hoc multiple-comparisons $p = 0.0099$ at 500 pA; (J) two-way ANOVA, $F(1, 23) = 15.47$, $p = 0.0007$). Middle panels, maximal firing rate; panel I: Veh = 20.14 ± 4.61; XE991 = 31.28 ± 8.53; $p < 0.0001$; panel J: Veh = 21.00 ± 2.63; PaTX1 = 26.92 ± 5.01; $p = 0.0029$). Right panels, current required to generate the maximum firing (I_{maxAP}): panel I: Veh = 428.57 ± 168.38 pA; XE991 = 538.89 ± 217.31 pA; $p = 0.1166$; panel J: Veh = 491.67 ± 90.03 pA; PaTX1 = 676.92 ± 238.59 pA; $p = 0.0107$). (K) Effect of co-application of RTG and NS5806 on neuronal excitability of LC neurons of 5xFAD mice (Veh: nine cells from three mice; RTG+NS5806: 14 cells from three mice). Left panel: current-spiking relationship (two-way ANOVA, $F(1, 21) = 12.35$, $p = 0.0021$). Middle panel: maximum firing rate (Veh = 28.56 ± 2.30; RTG+NS5806 = 22.36 ± 4.53; $p = 0.0027$). Right panel, I_{maxAP}. (Veh = 822.22 ± 171.59 pA; RTG+NS5806 = 614.29 ± 203.27 pA; $p = 0.0201$). (L) Effect of co-application of RTG and NS5806 on tonic firing of LC neurons in 5xFAD mice (Veh: eight cells from three mice; RTG+NS5806: 10 cells from three mice). Left panel, tonic firing rate (Veh = 9.64 ± 2.96 Hz; RTG+NS5806 = 4.81 ± 2.03 Hz; $p = 0.0014$). Right panel, resting membrane potential (Veh = −49.75 ± 3.20 mV; RTG+NS5806 = −53.20 ± 4.37 mV; $p = 0.1144$). Data are shown as mean ± SEM. Mann–Whitney tests were performed. HT, high threshold; LC, locus coeruleus; LT, low threshold; RTG, retigabine; Veh, vehicle; WT, wild type.

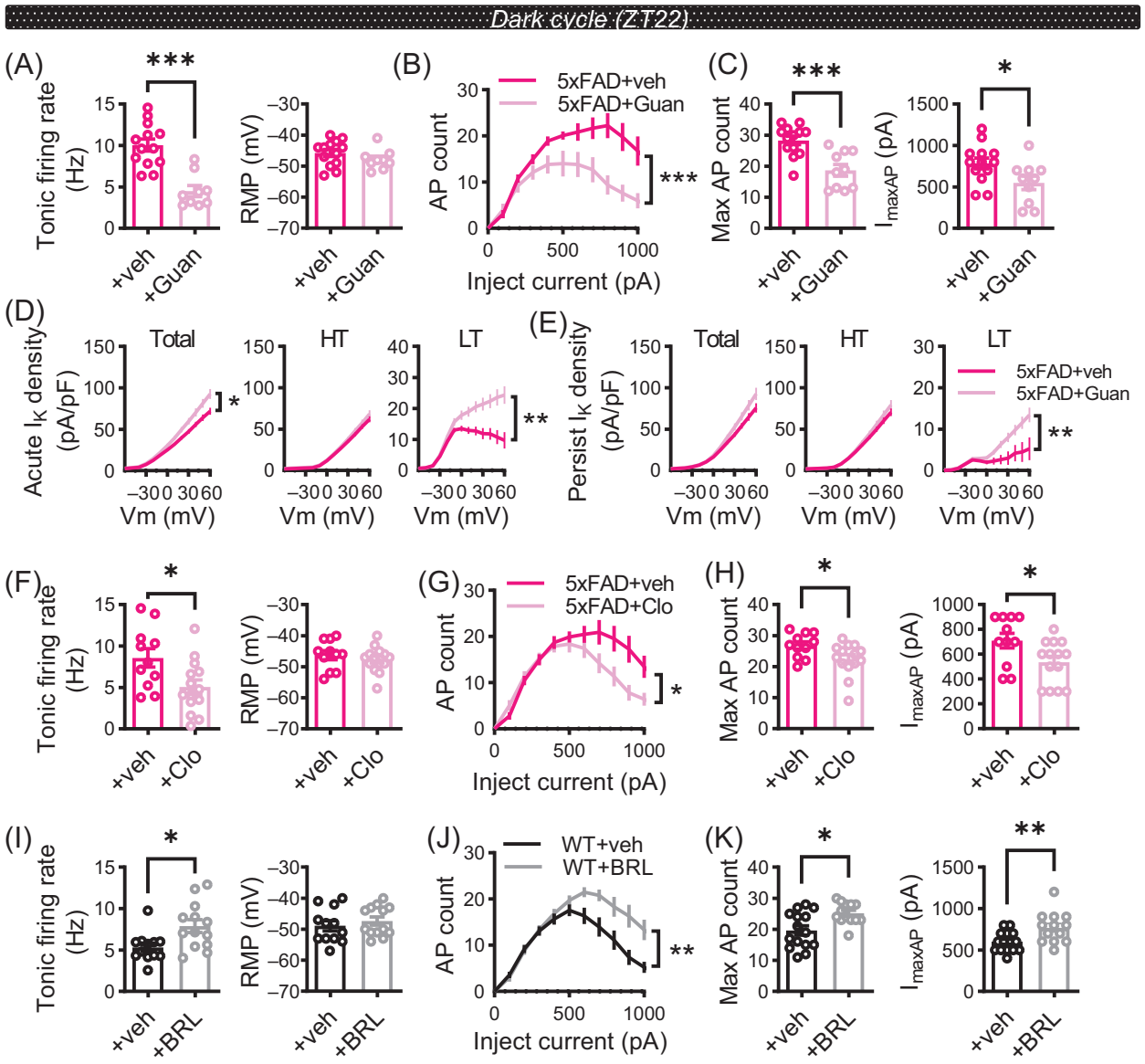

FIGURE 4 Activation of α2A adrenergic receptor restores Kv channel conductance and LC neuron activity in young 5xFAD mice. (A–C) Effect of Guan on tonic firing (A) and neuronal excitability (B and C) of LC neurons in 5xFAD mice (A), Veh: 13 cells from three mice; Guan: nine cells from three mice; (B and C) Veh: 13 cells from 3 mice; Guan: 10 cells from 3 mice) (A) Left panel: tonic firing rate (Veh = 10.04 ± 2.62 Hz; Guan = 4.49 ± 2.02 Hz; $p = 0.0001$). Right panel, resting membrane potential (Veh = −45.77 ± 3.94 mV; Guan = −47.67 ± 3.14 mV; $p = 0.2259$). (B) Current-spiking relationship (two-way ANOVA, F(1, 21) = 14.65, $p = 0.0010$). (C) Left panel, maximum firing rate (Veh = 28.31 ± 4.91; Guan = 18.70 ± 5.98; $p = 0.0009$). Right panel: I_{maxAP} (Veh = 784.62 ± 233.97 pA; Guan = 550.00 ± 254.95 pA; $p = 0.0272$). (D and E) Effect of Guan on acute I_k. (D) Persistent I_k (E) of LC neurons in 5xFAD mice (Veh: 15 cells from four mice; Guan: 22 cells from five mice). Left panels, total I_k; middle panels: HT I_k; right panels, LT I_k. (Two-way ANOVA: panel D: left: F(1, 35) = 5.487; $p = 0.0250$; middle: F(1, 35) = 1.109; $p = 0.2996$; right: F(1, 35) = 11.21; $p = 0.0020$; panel E, left: F(1, 35) = 3.326; $p = 0.0767$; middle: F(1, 35) = 1.190; $p = 0.2828$; right: F(1, 35) = 8.907; $p = 0.0052$). (F and H) Effect of application of clonidine (Clo) on tonic firing (F) and neuronal excitability (G), (H) of LC neurons of 5xFAD mice (Veh: 11 cells from three mice; Clo: 14 cells from three mice). (F) Left panel, tonic firing rate (Veh = 8.56 ± 3.70 Hz; Clo = 5.05 ± 3.21 Hz; $p = 0.0287$). Right panel, resting membrane potential (Veh = −46.27 ± 4.73 mV; Clo = −47.71 ± 4.08 mV; $p = 0.3634$). (G and H) (G) current-spiking relationship (two-way ANOVA, F(1, 23) = 6.276, $p = 0.0198$). (H) Left panel: maximum firing rate (Veh = 26.82 ± 3.92; Clo = 22.43 ± 5.26; $p = 0.0315$). Right panel: I_{maxAP} (Veh = 709.09 ± 197.25 pA; Clo = 535.71 ± 173.68 pA; $p = 0.0257$). (I–K) Effect of BRL on tonic firing (I) and neuronal excitability (J), (K) of LC neurons in WT mice (I), Veh: 12 cells from three mice; BRL: 13 cells from three mice; (J), (K), Veh: 15 cells from three mice; BRL: 13 cells from three mice). (I) Left panel: tonic firing rate (Veh = 5.33 ± 1.76 Hz; BRL = 7.89 ± 2.77 Hz; $p = 0.0220$). Right panel: resting membrane potential (Veh = −48.92 ± 5.57 mV; BRL = −47.39 ± 4.77 mV; $p = 0.5112$). (J and K) (J), current-spiking relationship (two-way ANOVA, F(1, 26) = 10.60, $p = 0.0031$). (K) Left panel: maximum firing rate (Veh = 19.67 ± 5.83; BRL = 25.15 ± 3.36; $p = 0.0171$). Right panel, I_{maxAP} (Veh = 600.00 ± 119.52 pA; BRL = 769.23 ± 184.32 pA; $p = 0.0088$). Data are shown as mean ± SEM. Mann–Whitney tests were performed. BRL, BRL-44408 maleate; Guan, guanfacine; HT, high threshold; LC, locus coeruleus; LT, low threshold; Veh, vehicle.

Kv4 and Kv7 conductance and producing LC hyperexcitability and hyperactivity specifically during the dark phase.

4.5 | Oligomeric Aβ induces defective α2A-AR-Kv channels signaling and drives LC abnormalities

We next sought to identify the pathological trigger underlying the early-onset LC abnormalities observed in young 5xFAD mice. Neuroinflammatory markers were minimal (Figure S5A–C) and amyloid plaque was absent in the LC region (Figure S1H), consistent with an early amyloidogenic stage. Nonetheless, direct quantification of Aβ42, the major toxic form of amyloid species implicated in AD, revealed a higher level of total Aβ42 in the LC-containing medial brainstem relative to several other regions, including basal forebrain, medulla, and visual cortex in 2-month-old 5xFAD mice (Figure S5D).

Oligomeric Aβ (AβO) is known to bind an allosteric site on α2A-ARs, aberrantly redirecting downstream signaling.[44] To test whether elevated AβO contributed to LC dysfunction, we pre-incubated acute LC slices from wildtype mice collected at ZT22 with 50 nM AβO prior to electrophysiological recording (Figure 5A). Compared with vehicle controls, AβO exposure significantly increased LC neuronal excitability (Figure 5B–D) and tonic firing rates (Figure 5E), producing WT neuronal phenotypes closely resembling those of young 5xFAD mice. AβO-treated WT neurons also exhibited reductions in both acute (Figure 5H) and persistent (Figure 5K) low-threshold Kv conductance, indicating that AβO alone is sufficient to impair Kv4/Kv7 channel function. Finally, application of the α2A-AR agonist guanfacine fully reversed the AβO-induced hyperexcitability and hyperactivity, demonstrating that α2A-AR lies downstream of AβO in mediating its deleterious effects on LC physiology.

Collectively, these results identify soluble Aβ oligomers as an early pathological trigger that impairs α2A-AR–Kv channel signaling, leading to persistent LC hyperexcitability that mirrors the phenotype of young 5xFAD mice.

4.6 | Restoration of sleep–wake disturbances in 5xFAD mice via local modulation of LC α2A-AR and Kv channel activity

Our previous findings demonstrated that impaired α2A-AR signaling and reduced downstream Kv4 and Kv7 channel conductance contributed to LC hyperactivity in young 5xFAD mice. To determine whether this signaling dysfunction underlies the early-onset sleep-wake abnormalities observed in this AD model, we employed pharmacological interventions targeting this pathway.

Guanfacine, a clinically approved α2A-AR agonist used to treat various neurological disorders,[45,46] was locally infused bilaterally into the LC of young 5xFAD mice via implanted cannulas immediately prior to the onset of the dark phase (Figure 6A; see "Methods"). Compared to vehicle controls, guanfacine significantly reduced wakefulness and increased NREM sleep during the dark phase (Figure 6B–G, Supplementary Table 4). In addition, guanfacine-treated mice exhibited a trend toward enhanced transitions between vigilance states (Figure S6A–C), suggesting improved sleep–wake flexibility. These results implicate LC α2A-AR signaling as a key regulator of arousal and sleep architecture and its dysfunction as a contributor to early-onset sleep disturbances in 5xFAD mice.

We next assessed whether direct activation of Kv channels could similarly restore normal sleep architecture. Retigabine, a Kv7 channel opener, was previously shown to reduce LC hyperexcitability *ex vivo* (Figure S6G–J). Local infusion of retigabine into the LC of 5xFAD mice during the dark phase significantly ameliorated hyperarousal and restored NREM sleep (Figure 6H–M and Table S5), mirroring the effects of guanfacine. These findings were further confirmed through systemic administration: A single IP injection of retigabine in 5xFAD mice significantly increased NREM sleep and the number of wake–NREM transitions during the dark phase (Figure S7A–M and Table S6), without altering NREM δ power (Figure S7H–J). Notably, the same treatment had only modest effects on sleep parameters in WT mice (Figure S8 and Table S7), suggesting a disease-specific therapeutic potential.

Together, these results support a mechanistic model in which LC hyperactivity – driven by disrupted α2A-AR signaling and impaired Kv channel function – plays a central role in the early manifestation of sleep–wake disturbances in AD. Pharmacological modulation of this pathway may represent a promising strategy for early intervention in AD-associated sleep pathology.

5 | DISCUSSION

Sleep–wake disturbances are increasingly recognized as an early and clinically significant feature of AD, often preceding the onset of cognitive decline by years. Hyperarousal, sleep fragmentation, and reduced total sleep time are frequently reported in both patients with early-stage AD and individuals at risk. These alterations are not merely epiphenomena of neurodegeneration but may actively contribute to the pathogenesis of AD by exacerbating Aβ accumulation and tau pathology through disrupted glymphatic clearance and elevated neuronal activity.[1,47–49] Thus, understanding the cellular and circuit-level mechanisms underlying early-onset sleep–wake dysregulation in AD is of both fundamental and translational importance.

Our results identify a key role for dysfunctional α2A-AR–mediated auto-inhibition via modulation of Kv 4 and 7 channel conductance in the hyperexcitability of LC neurons in young 5xFAD mice, particularly during the dark (wake-dominant) phase. Under normal physiological conditions, α2A-ARs act as presynaptic[50] and somatodendritic[51] autoreceptors that are activated by elevated extracellular NE levels, typically during periods of sustained LC activity. These receptors are Gi/o-coupled G protein–coupled receptors (GPCRs) that inhibit further neuronal firing and NE release. However, NE release from somatic sites occurs predominantly at high LC firing rates (>15 Hz), whereas low-frequency activity (<4 Hz) produces sparse somatic NE release.[51,52] This supports the model in which somatic α2A-ARs primarily function

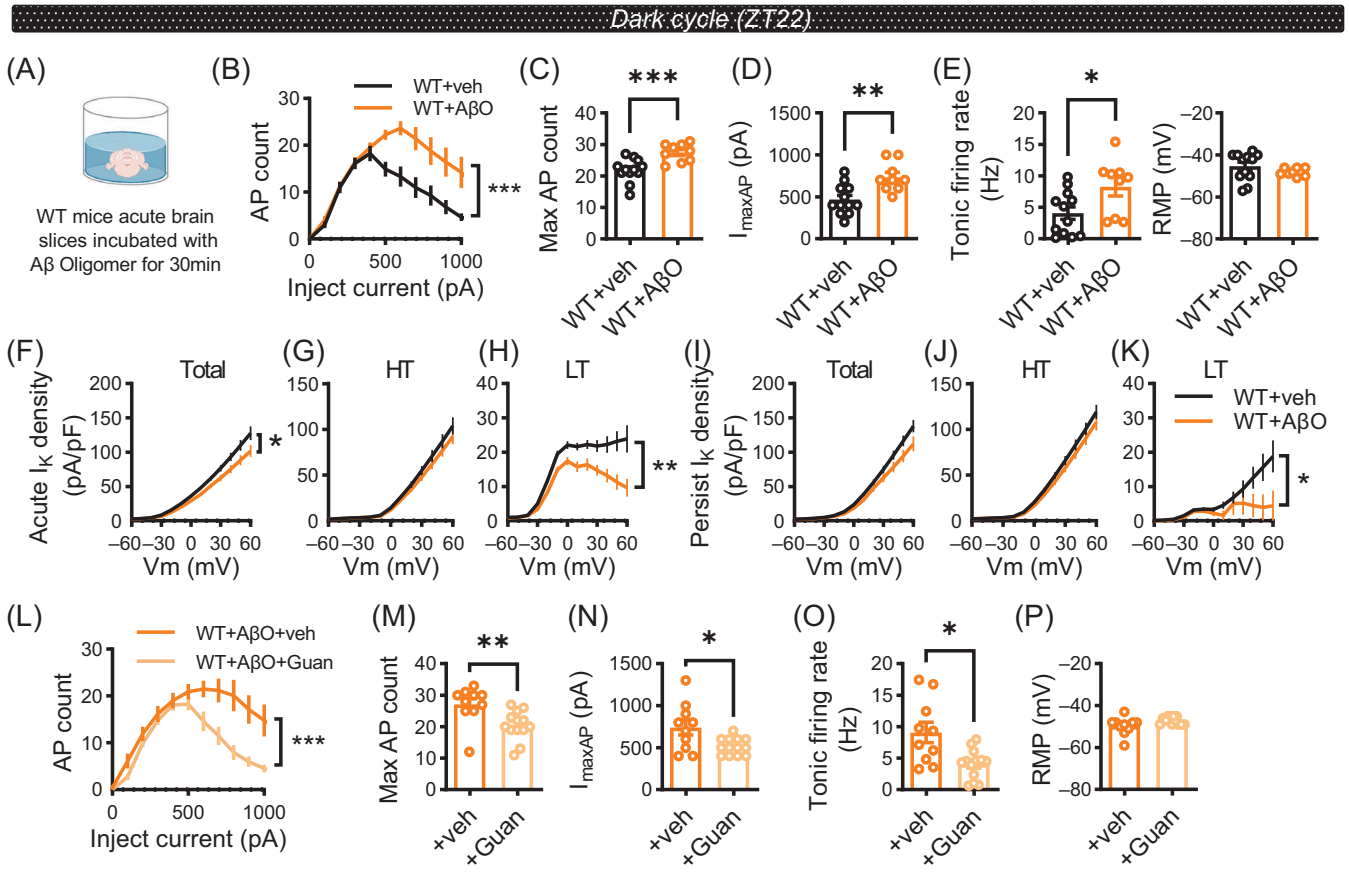

FIGURE 5 AβO elevates WT LC neuronal excitability and tonic activity. (A) Schematic diagram showing the pre-incubation of WT mice acute brain slices with 50 nM Aβ oligomer for 30 min. (B–E) Effect of Aβ oligomer on neuronal excitability (B–D) and tonic firing (E) of LC neurons in WT mice (Veh: 12 cells from three mice; AβO: nine cells from three mice). (B–D) (B) Current-spiking relationship (two-way ANOVA, F(1, 19) = 15.98, $p = 0.0008$). (C) Maximum firing rate (Veh = 21.83 ± 3.61; AβO = 27.44 ± 2.88; $p = 0.0008$). (D) I_{maxAP} (Veh = 466.67 ± 177.53 pA; AβO = 733.33 ± 173.21 pA; $p = 0.0042$). (E) Left panel: tonic firing rate (Veh = 4.069 ± 3.50 Hz; AβO = 8.26 ± 4.44 Hz; $p = 0.0227$). Right panel: resting membrane potential (Veh = −45.33 ± 6.61 mV; AβO = −48.10 ± 1.83 mV; $p = 0.2367$). (F–K) Comparison of Kv channel conductance of LC neurons between Veh- or AβO-treated WT mice (Veh:13 cells from three mice; AβO: 10 cells from three mice). *V*-I_k curves of acute (F–H) and persistent (I–K) I_k density. (F and I) Total I_k. (G and J) HT I_k. (H and K) LT I_k. (Two-way ANOVA, (F) F(1, 21) = 4.340; $p = 0.0496$; (G) F(1, 21) = 0.8961; $p = 0.3546$; (H) F(1, 21) = 10.86; $p = 0.0034$; (I) F(1, 21) = 3.373; $p = 0.0805$; (J) F(1, 21) = 1.096; $p = 0.3070$; (K) F(1, 21) = 4.439; $p = 0.0473$). (L–P) Effect of Guan on neuronal excitability (L–N) and tonic firing (O and P) of Aβ oligomer pre-incubated LC neurons in WT mice (Veh: 10 cells from three mice; Guan: 13 cells from three mice). (L–N) (L) Current-spiking relationship (two-way ANOVA, F(1, 21) = 15.40, $p = 0.0008$). (M) Maximum firing rate (Veh = 27.10 ± 5.90; Guan = 20.46 ± 4.63; $p = 0.0020$). (N) I_{maxAP} (Veh = 740.00 ± 283.63 pA; Guan = 515.39 ± 98.71 pA; $p = 0.0402$). (O) Tonic firing rate (Veh = 9.07 ± 5.11 Hz; Guan = 4.05 ± 2.34 Hz; $p = 0.0121$). (P) Resting membrane potential (Veh = -49.70 ± 4.16 mV; Guan = −47.00 ± 1.78 mV; $p = 0.0649$). Data are shown as mean ± SEM. Mann–Whitney tests were performed. AβO, oligomeric amyloid beta; Guan, guanfacine; HT, high threshold; LC, locus coeruleus; LT, low threshold; Veh, vehicle; WT, wild type.

during arousal-dominant dark period when LC neurons are more active (Figure 2D,G).[6,8] In line with this model, our data show that in 5xFAD mice, the impaired α2A-AR function leads to pronounced hyperactivity of LC neurons only during the dark phase. In contrast, the light phase, characterized by lower overall LC activity and NE release, remains largely unaffected, masking the defect in α2A-AR signaling during this period.

Although significant reductions in α2A-AR mRNA and its binding sites have been reported in the LC of AD patients at later stages,[53] our data suggest that functional impairment of α2A-AR signaling precedes these transcriptional and translational changes (Figure S4M,N). Guanfacine dose–response experiments performed at ZT9, when α2A-AR occupancy is minimal, reveal significantly reduced receptor activation efficacy in 5xFAD LC neurons. At this early stage, the deficit may be due to post-translational mechanisms, such as abnormal receptor phosphorylation,[54] membrane trafficking, or downregulation of interacting proteins.[55] Low levels of Aβ accumulation and early-stage neuroinflammation may contribute to this dysfunction by altering receptor localization or stability.[56,57] Notably, AβO has been shown to bind to an allosteric site on α2-ARs and redirect downstream signaling[44]. In line with this, acute exposure of WT LC slices to low concentrations of AβO induced 5xFAD-like LC neuronal hyperexcitability and hyperactivity, an effect fully rescued by α2A-AR activation with guanfacine. These results support a model in which competitive

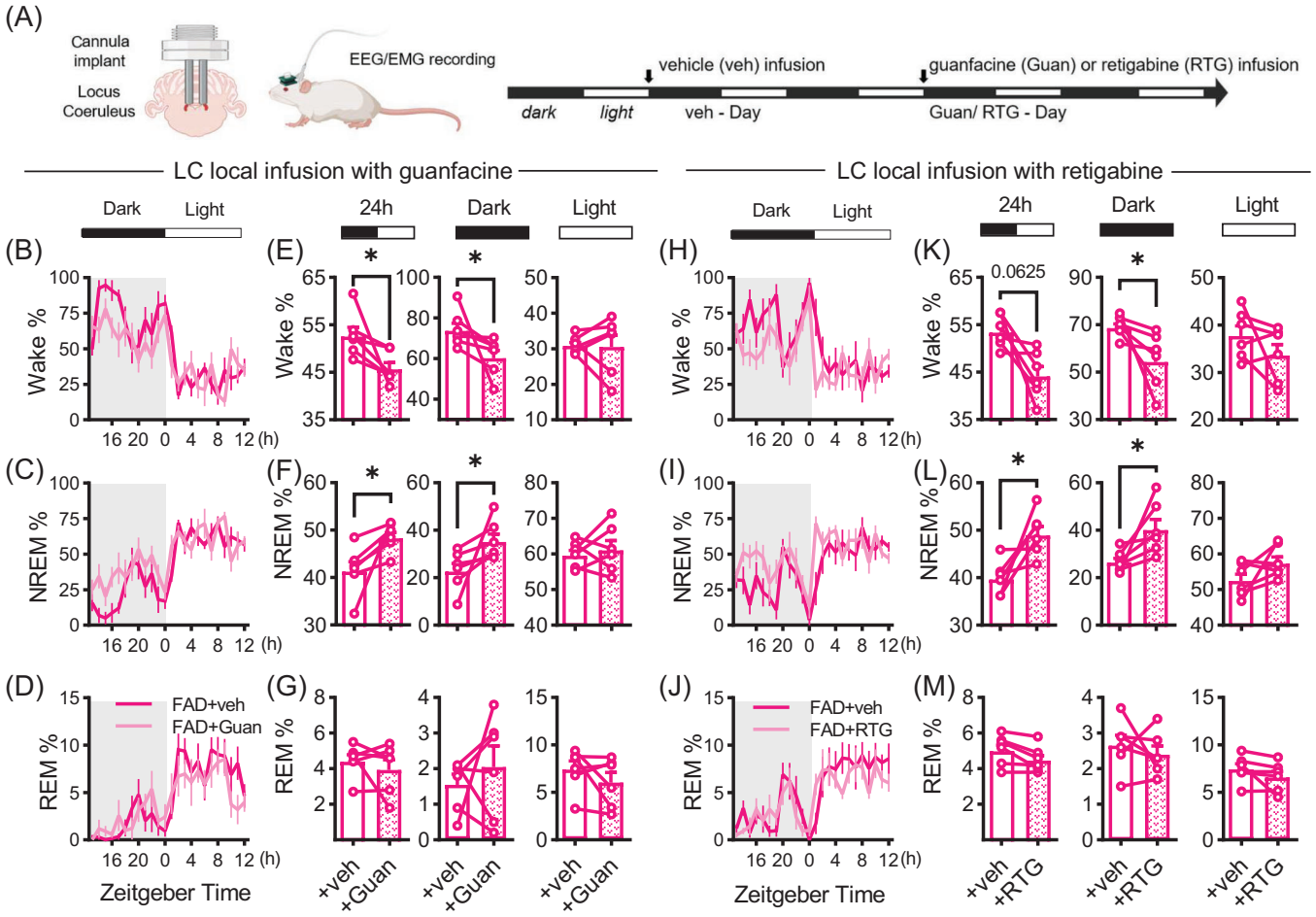

FIGURE 6 Local infusion of Guan or retigabine alleviates the sleep-wake disturbances in 2-month-old 5xFAD mice. (A) Schematic diagram showing experimental design of cannula implantation in LC and the EEG/EMG recording timeline to evaluate effect of Guan or retigabine on sleep pattern. (B–G) Comparisons of percentages of time spent in wake (upper panels), NREM (middle panels), and REM (lower panels) immediately after drugs (Veh, opened bars; guanfacine: Guan, patterned bars) infusion through cannula implanted in LC at ZT12 (Arrow) in 5xFAD mice. (B–D) Percentages of time spent in wake (B), NREM (C), and REM (D) across the light/dark cycle. (E–G) Percentages in the 24-h day (left panels), the dark cycle (middle panels) and the light cycle (right panels) were analyzed (5xFAD: $n = 6$ mice). Data shown in Table S4. (H–M) Comparisons of percentages of time spent in wake (upper panels), NREM sleep (middle panels), and REM sleep (lower panels) immediately after drugs (Veh, opened bars; RTG, patterned bars) infusion into LC areas of 5xFAD mice at ZT12. (H)–(J), Percentages of time spent in wake (H), NREM sleep (I), and REM sleep (J) across light/dark cycle. (K–M) Percentages in 24-h day (left panels), dark cycle (middle panels) and light cycle (right panels) were analyzed (5xFAD: $n = 6$ mice). Data shown in Table S5. Data are shown as mean ± SEM. Wilcoxon signed-rank tests were performed. EEG, electroencephalogram; EMG, electromyogram; GUAN, guanfacine; LC, locus coeruleus; NREM, non-rapid eye movement; REM, rapid eye movement; RTG, retigabine; Veh, vehicle.

interference by AβO contributes to early α2A-AR dysfunction in LC neurons.

Mechanistically, we found that α2A-AR activation enhances the conductance of both Kv4 and Kv7 channels, and this enhancement is sufficient to suppress the hyperexcitability of LC neurons in young 5xFAD mice. These findings point to the importance of intact α2A-AR–Kv channel coupling in maintaining LC excitability and proper sleep–wake architecture. As a GPCR, α2A-AR activation promotes the dissociation of Gβγ subunits,[58] which has been shown to directly bind to and increase the open probability of Kv7 channel,[42] thereby dampening neuronal excitability.

Importantly, Kv dysfunction is commonly observed in aging and diseases.[59,60] Both Kv4 and Kv7 channels have been implicated in pathological neuronal hyperexcitability and seizures when their function is compromised.[61–63] Notably, reduced Kv7 activity in hypothalamic hypocretin (Hcrt) neurons has been shown to promote hyperexcitability and sleep disruption in aged mice,[64] supporting a broader role for Kv dysfunction in sleep and arousal disturbances.

Beyond direct α2A-AR signaling deficits, other mechanisms may contribute to the impaired Kv channel function observed in early AD model. These include post-translational modifications that alter channel kinetics,[65,66] downregulation of auxiliary or interacting proteins necessary for channel function,[67] disrupted subcellular trafficking and localization of Kv channels,[68] and changes in the microenvironment and signaling pathways that modulate channel expression or activity.[69] As more drugs targeting Kv channels become available,[70] in-depth

analysis of which and how Kv channels are dysregulated in early AD will become necessary.

The sleep–wake disturbances observed in 5xFAD mice – hyperarousal, inflexible state transitions, and prolonged wake bouts – mirror clinical observations in individuals with mild cognitive impairment (MCI) and prodromal AD. In human studies, early-stage AD patients frequently exhibit elevated arousal levels, increased sleep latency, and heightened anxiety symptoms.[71,72] LC hyperactivity may be a converging mechanism underlying these phenotypes, as the LC mediates arousal, stress reactivity, and anxiety via widespread NE projections to the cortex, hippocampus, and amygdala.[8,73] More importantly, the initial hyperactivity of LC neurons may have long-term consequences for AD progression.[71,72] A recent finding indicates that the hyperactivity of LC neurons in amyloid precursor protein (APP) knock-in mice leads to the early degradation of LC fibers in the olfactory bulb that drives the olfactory dysfunction.[74] These observations position early LC hyperactivity as both a biomarker and a potential driver of AD progression.

Taken together, our findings highlight the pivotal role of LC dysregulation – specifically α2A-AR signaling deficits and associated Kv channel dysfunction – in mediating early sleep–wake disturbances in AD. Therapeutically, restoring LC auto-inhibition or directly targeting LC hyperexcitability may represent promising early interventions to alleviate arousal dysregulation associated with the prodromal phase.

AUTHOR CONTRIBUTIONS

Conceptualization: Kai-Wen He. Primary investigation: Yi-Ci Zhang. Assistant investigation: Xue-Ting Zhang, Peng-Yue Chen, Zi-Yue Zhou, and Mao-Qing Huang. Data analysis: Yi-Ci Zhang, Xue-Ting Zhang, and Zi-Yue Zhou. Writing: Yi-Ci Zhang and Kai-Wen He. Funding acquisition: Kai-Wen He. Supervision: Kai-Wen He

ACKNOWLEDGMENTS

The authors thank the staff members of the animal facility at the National Facility for Protein Science in Shanghai (NFPS), Shanghai Advanced Research Institute, Chinese Academy of Sciences, China, for their excellent support. This work was supported by Shanghai Science and Technology Development Funds (Grant No. 22ZR1475100), NSFC (Grant No. 32070963, 32271004), Lingang Laboratory (Grant No. LG-ADB410101), and Shanghai Municipal Science and Technology Major Project (Grant No. 2019SHZDZX02) to Kai-Wen He.

CONFLICT OF INTEREST STATEMENT

The authors declare no competing interests.

ORCID

Kai-Wen He https://orcid.org/0000-0002-1187-098X

REFERENCES

1. Kent B, Feldman H, Nygaard H. Sleep and its regulation: an emerging pathogenic and treatment frontier in Alzheimer's disease. *Prog Neurobiol*. 2021;197:101902.
2. Mander B, Winer J, Jagust W, Walker M. Sleep: A novel mechanistic pathway, biomarker, and treatment target in the pathology of Alzheimer's disease?. *Trends Neurosci*. 2016;39:552-566.
3. Wang C, Holtzman D. Bidirectional relationship between sleep and Alzheimer's disease: Role of amyloid, tau, and other factors. *Neuropsychopharmacology*. 2019;45:104-120.
4. Zhang Y, Ren R, Yang L, et al. Sleep in Alzheimer's disease: A systematic review and meta-analysis of polysomnographic findings. *Translational Psychiatry*. 2022;12(1):136.
5. Shi L, Chen S, Ma M, et al. Sleep disturbances increase the risk of dementia: A systematic review and meta-analysis. *Sleep Med Rev*. 2018;40:4-16.
6. Aston-Jones G, Bloom F. Activity of norepinephrine-containing locus coeruleus neurons in behaving rats anticipates fluctuations in the sleep-waking cycle. *J Neurosci*. 1981;1:876-886.
7. Osorio-Forero A, Cherrad N, Banterle L, Fernandez L, Luthi A. When the locus coeruleus speaks up in sleep: Recent insights, emerging perspectives. *Int J Mol Sci*. 2022;23.
8. Poe GR, Foote S, Eschenko O, et al. Locus coeruleus: A new look at the blue spot. *Nat Rev Neurosci*. 2020;21:644-659.
9. Lüthi A, Nedergaard M. Anything but small: Microarousals stand at the crossroad between noradrenaline signaling and key sleep functions. *Neuron*. 2025;113(4):509-523.
10. Carter ME, Yizhar O, Chikahisa S, et al. Tuning arousal with optogenetic modulation of locus coeruleus neurons. *Nat Neurosci*. 2010;13:1526-1533.
11. Silverman D, Chen C, Chang S,etal. Activation of locus coeruleus noradrenergic neurons rapidly drives homeostatic sleep pressure. *Science Advances*. 2025;11.
12. Jacobs HIL, Becker JA, Kwong K, et al. In vivo and neuropathology data support locus coeruleus integrity as indicator of Alzheimer's disease pathology and cognitive decline. *Sci Transl Med*. 2021;13:eabj2511.
13. Wilson RS, Nag S, Boyle PA, et al. Neural reserve, neuronal density in the locus ceruleus, and cognitive decline. *Neurology*. 2013;80:1202-1208.
14. Prokopiou PC, Engels-Domínguez N, et al. Lower novelty-related locus coeruleus function is associated with Aβ-related cognitive decline in clinically healthy individuals. *Nat Commun*. 2022;13:1571.]
15. Braak H, Del Tredici K. The pathological process underlying Alzheimer's disease in individuals under thirty. *Acta Neuropathol*. 2011;121:171-181.
16. Braak H, Thal D, Ghebremedhin E, Del Tredici K. Stages of the pathologic process in Alzheimer disease: Age categories from 1 to 100 years. *J Neuropathol Exp Neurol*. 2011;70:960-969.
17. Zong F, Min X, Zhang Y, et al. Circadian time- and sleep-dependent modulation of cortical parvalbumin-positive inhibitory neurons. *EMBO J*. 2023;42:e111304.
18. Min X, Wang J, Zong F, Zhao J, Liu N, He K. miR-34a regulates silent synapse and synaptic plasticity in mature hippocampus. *Prog Neurobiol*. 2023;222:102404.
19. Bridi MC, Zong F, Min X, et al. Daily oscillation of the excitation-inhibition balance in visual cortical circuits. *Neuron*. 2020;105:621-629 e624.
20. Wang J, Ma GM, Tang XQ, et al. Brain region-specific synaptic function of FUS underlies the FTLD-linked behavioural disinhibition. *Brain*. 2022;146(5).
21. Dobin A, Davis CA, Schlesinger F, et al. STAR: ultrafast universal RNA-seq aligner. *Bioinformatics*. 2013;29:15-21.
22. Li B, Dewey C. RSEM: accurate transcript quantification from RNA-Seq data with or without a reference genome. *BMC Bioinformatics*. 2011;12:323.
23. Love M, Huber W, Anders S. Moderated estimation of fold change and dispersion for RNA-seq data with DESeq2. *Genome Biol*. 2014;15:550.

24. Holth J, Mahan T, Robinson G, Rocha A, Holtzman D. Altered sleep and EEG power in the P301S Tau transgenic mouse model. *Ann Clin Transl Neurol*. 2017;4:180-190.
25. Jyoti A, Plano A, Riedel G, Platt B. EEG, activity, and sleep architecture in a transgenic Aβ PPswe/PSEN1A246E Alzheimer's disease mouse. *J Alzheimers Dis*. 2010;22:873-887.
26. Sethi M, Joshi S, Webb R, et al. Increased fragmentation of sleep-wake cycles in the 5xfad mouse model of Alzheimer's disease. *Neuroscience*. 2015;290:80-89.
27. Bianchetti A, Scuratti A, Zanetti O, et al. Predictors of mortality and institutionalization in Alzheimer disease patients 1 year after discharge from an Alzheimer dementia unit. *Dementia*. 1995;6:108-112.
28. Guarnieri B, Adorni F, Musicco M, et al. Prevalence of sleep disturbances in mild cognitive impairment and dementing disorders: a multicenter Italian clinical cross-sectional study on 431 patients. *Dement Geriatr Cogn Disord*. 2012;33:50-58.
29. . Oakley H, Cole SL, Logan S, et al. Intraneuronal beta-amyloid aggregates, neurodegeneration, and neuron loss in transgenic mice with five familial Alzheimer's disease mutations: potential factors in amyloid plaque formation. *J Neurosci*. 2006;26:10129-10140.
30. Scarpa JR, Jiang P, Gao VD, Vitaterna MH, Turek FW, Kasarskis A. NREM delta power and AD-relevant tauopathy are associated with shared cortical gene networks. *Sci Rep*. 2021;11:7797.
31. Osorio-Forero A, Foustoukos G, Cardis R, et al. Infraslow noradrenergic locus coeruleus activity fluctuations are gatekeepers of the NREM–REM sleep cycle. *Nature Neuroscience*. 2024;28:84-96.
32. Johnston J, Forsythe I, Kopp-Scheinpflug C. Going native: voltage-gated potassium channels controlling neuronal excitability. *J Physiol*. 2010;588:3187-3200.
33. Chagot B, Escoubas P, Villegas E, et al. Solution structure of Phrixotoxin 1, a specific peptide inhibitor of Kv4 potassium channels from the venom of the theraphosid spider Phrixotrichus auratus. *Protein Sci*. 2004;13:1197-1208.
34. Wang J, Long C, Li KY, Xu HT, Yuan LL, Wu GY. Potent block of potassium channels by MEK inhibitor U0126 in primary cultures and brain slices. *Scientific Reports*. 2018;8(1).
35. Yuan L, Chen X, Kunjilwar K, Pfaffinger P, Johnston D. Acceleration of K+ channel inactivation by MEK inhibitor U0126. *American Journal of Physiology-Cell Physiology*. 2006;290:C165-C171.
36. Gilsbach R, Hein L. Are the pharmacology and physiology of α_2 adrenoceptors determined by α_2-heteroreceptors and autoreceptors respectively?. *Br J Pharmacol*. 2012;165:90-102.
37. Knaus A, Muthig V, Schickinger S, et al. Alpha2-adrenoceptor subtypes–unexpected functions for receptors and ligands derived from gene-targeted mouse models. *Neurochem Int*. 2007;51:277-281.
38. Silverman D, Chen C, Chang S, et al. Activation of locus coeruleus noradrenergic neurons rapidly drives homeostatic sleep pressure. *Sci Adv*. 2025;11:eadq0651.
39. García-Díaz G, et al. Alpha(2)-adrenergic receptor activation reinstates motor deficits in rats recovering from cortical injury. *Neural Regen Res*. 2023;18:875-880.
40. Silverman D, et al. Activation of locus coeruleus noradrenergic neurons rapidly drives homeostatic sleep pressure. *bioRxiv*. 2024.
41. van der Horst J, Greenwood I, Jepps T. Cyclic AMP-Dependent regulation of Kv7 voltage-gated potassium channels. *Front Physiol*. 2020;11:727.
42. Stott J, Greenwood I. G protein $\beta\gamma$ regulation of KCNQ-encoded voltage-dependent K channels. *Front Physiol*. 2024;15:1382904.
43. Stott J, Povstyan O, Carr G, Barrese V, Greenwood I. G-protein $\beta\gamma$ subunits are positive regulators of Kv7.4 and native vascular Kv7 channel activity. *Proc Natl Acad Sci U S A*. 2015;112:6497-6502.
44. Zhang F, Gannon M, Chen Y, et al. beta-amyloid redirects norepinephrine signaling to activate the pathogenic GSK3beta/tau cascade. *Sci Transl Med*. 2020;12.
45. Dalmaijer ES, Li KMS, Gorgoraptis N, et al. Randomised, double-blind, placebo-controlled crossover study of single-dose guanfacine in unilateral neglect following stroke. *J Neurol Neurosurg Psychiatry*. 2018;89:593-598.
46. McCracken JT, McGough JJ, Loo SK, et al. Combined stimulant and guanfacine administration in attention-deficit/hyperactivity disorder: A controlled, comparative study. *J Am Acad Child Adolesc Psychiatry*. 2016;55:657-666 e651.
47. Jiang-Xie L, Drieu A, Kipnis J. Waste clearance shapes aging brain health. *Neuron*. 2024.
48. Casagrande M, Forte G, Favieri F, Corbo I. Sleep quality and aging: A systematic review on healthy older people, mild cognitive impairment and Alzheimer's disease. *Int J Environ Res Public Health*. 2022;19:8457.
49. Lucey BP, Wisch J, Boerwinkle AH, et al. Sleep and longitudinal cognitive performance in preclinical and early symptomatic Alzheimer's disease. *Brain*. 2021;144:2852-2862.
50. Trendelenburg A, Limberger N, Starke K. Presynaptic ?2-autoreceptors in brain cortex: ?2D in the rat and ?2A in the rabbit. *Naunyn-Schmiedeberg's Archives of Pharmacology*. 1993;348:35-45.
51. Huang H, Wang S, Yao W, et al. Long latency of evoked quantal transmitter release from somata of locus coeruleus neurons in rat pontine slices. *Proc Natl Acad Sci U S A*. 2007;104:1401-1406.
52. Huang H, Zhu F, Chen X, Xu ZD, Zhang CX, Zhou Z. Physiology of quantal norepinephrine release from somatodendritic sites of neurons in locus coeruleus. *Front Mol Neurosci*. 2012;5:29.
53. Szot P, White SS, Greenup JL, Leverenz JB, Peskind ER, Raskind MA. Compensatory changes in the noradrenergic nervous system in the locus ceruleus and hippocampus of postmortem subjects with Alzheimer's disease and dementia with lewy bodies. *The Journal of Neuroscience*. 2006;26:467-478.
54. Liang M, Eason MG, Jewell-Motz EA, et al. Phosphorylation and functional desensitization of the alpha2A-adrenergic receptor by protein kinase C. *Mol Pharmacol*. 1998;54:44-49.
55. Xu J, Chen Y, Lu R, Cottingham C, Jiao K, Wang Q. Protein kinase A phosphorylation of spinophilin modulates its interaction with the alpha 2A-adrenergic receptor (AR) and alters temporal properties of alpha 2AAR internalization. *J Biol Chem*. 2008;283:14516-14523.
56. Xu H, Rajsombath M, Weikop P, Selkoe D. Enriched environment enhances beta-adrenergic signaling to prevent microglia inflammation by amyloid-beta. *EMBO Mol Med*. 2018;10.
57. Tamulytė R, Baronaitė I, Šulskis D, Smirnovas V, Jankunec M. Pro-inflammatory S100A8 protein exhibits a detergent-like effect on anionic lipid bilayers, as imaged by high-speed AFM. *ACS Appl Mater Interfaces*. 2025;17:2635-2647.
58. . Knight KM, Ghosh S, Campbell SL, et al. A universal allosteric mechanism for G protein activation. *Mol Cell*. 2021;81:1384-1396 e1386.
59. Subramaniam M, Althof D, Gispert S, et al. Mutant α-synuclein enhances firing frequencies in dopamine substantia nigra neurons by oxidative impairment of A-type potassium channels. *J Neurosci*. 2014;34:13586-13599.
60. Hu J, Malloy C, Liu Y, et al. Activity-dependent degradation of Kv4.2 contributes to synaptic plasticity and behavior in Angelman syndrome model mice. *Cell Rep*. 2025;44:115583.
61. Barnwell LFS, Lugo JN, Lee WL, et al. Kv4.2 knockout mice demonstrate increased susceptibility to convulsant stimulation. *Epilepsia*. 2009;50:1741-1751.
62. Tiwari D, Schaefer TL, Schroeder-Carter LM, et al. The potassium channel Kv4.2 regulates dendritic spine morphology, electroencephalographic characteristics and seizure susceptibility in mice. *Exp Neurol*. 2020;334:113437.
63. Nappi P, Miceli F, Soldovieri MV, Ambrosino P, Barrese V, Taglialatela M. Epileptic channelopathies caused by neuronal Kv7 (KCNQ) channel dysfunction. *Pflugers Arch*. 2020;472:881-898.

64. Li S, Damonte VM, Chen C, et al. Hyperexcitable arousal circuits drive sleep instability during aging. *Science*. 2022;375:eabh3021.
65. Cerda O, Trimmer J. Analysis and functional implications of phosphorylation of neuronal voltage-gated potassium channels. *Neurosci Lett*. 2010;486:60-67.
66. Salzer I, Erdem FA, Chen W, et al. Phosphorylation regulates the sensitivity of voltage-gated Kv7.2 channels towards phosphatidylinositol-4,5-bisphosphate. *J Physiol*. 2017;595:759-776.
67. Wu L, Song Y, Zhang C, Liu JK. Channel-interacting proteins in the neurological and cardiovascular systems: An updated review. *Cells*. 2023;12:1894.
68. Xia X, Zhang Q, Jia Y, et al. Molecular basis and restoration of function deficiencies of Kv7.4 variants associated with inherited hearing loss. *Hear Res*. 2020;388:107884.
69. Greene D, Hoshi N. Modulation of Kv7 channels and excitability in the brain. *Cell Mol Life Sci*. 2017;74:495-508.
70. Barrese V, Stott J, Greenwood I. KCNQ-encoded potassium channels as therapeutic targets. *Annu Rev Pharmacol Toxicol*. 2018;58:625-648.
71. Jain R, Chepke C, Davis L, McIntyre R, Raskind M. Dysregulation of noradrenergic activity: its role in conceptualizing and treating major depressive disorder, schizophrenia, agitation in Alzheimer's disease, and posttraumatic stress disorder. *J Clin Psychiatry*. 2024;85:57634.
72. Chalermpalanupap T, Schroeder JP, Rorabaugh JM, et al. Locus coeruleus ablation exacerbates cognitive deficits, neuropathology, and lethality in P301S tau transgenic mice. *J Neurosci*. 2018;38:74-92.
73. Berridge C, Waterhouse B. The locus coeruleus-noradrenergic system: Modulation of behavioral state and state-dependent cognitive processes. *Brain Res Brain Res Rev*. 2003;42:33-84.
74. Meyer C, Niedermeier T, Feyen PLC, et al. Early locus coeruleus noradrenergic axon loss drives olfactory dysfunction in Alzheimer's disease. *Nature Communications*. 2025;16.

SUPPORTING INFORMATION

Additional supporting information can be found online in the Supporting Information section at the end of this article.

How to cite this article: Zhang Y-C, Zhang X-T, Chen P-Y, Zhou Z-Y, Huang M-Q, He K-W. Impaired adrenergic regulation of Kv channels underlies LC hyperactivity and early-onset sleep disruption in AD-like amyloidogenic mice. *Alzheimer's Dement*. 2026;22:e71127. https://doi.org/10.1002/alz.71127